PASJ: Publ. Astron. Soc. Japan **55**, 59–74, 2003 February 25

The Virgo High-Resolution CO Survey: II. Rotation Curves and Dynamical Mass Distributions

Yoshiaki SOFUE,[1] Jin KODA,[1,2] Hiroyuki NAKANISHI,[1] and Sachiko ONODERA[1]
[1]*Institute of Astronomy, The University of Tokyo, Mitaka, Tokyo 181-0015*
[2]*Nobeyama Radio Observatory, National Astronomical Observaroty, Minamimaki, Minamisaku, Nagano 384-1305*
sofue@ioa.s.u-tokyo.ac.jp

(Received 2002 September 1; accepted 2002 December 24)

Abstract

Based on a high-resolution CO survey of Virgo spirals with the Nobeyama Millimeter-wave Array, we determined the dynamical centers using velocity fields, and derived position–velocity diagrams (PVDs) along the major axes of the galaxies across their dynamical centers. We applied a new iteration method to derive rotation curves (RCs), which reproduce the observed PVDs. The obtained high-accuracy RCs generally show a steep rise in the central ~ 100 to 200 pc regions, followed by flat rotation in the disk. We applied a deconvolution method to calculate the surface-mass density (SMD) using the RCs based on two extreme assumptions that the mass distribution is either spherical or thin-disk shaped. Both assumptions give nearly identical results, agreeing with each other within a factor of two at any radii. The SMD distributions revealed central massive cores with peak SMD of $\sim 10^4$–$10^5\,M_\odot\,\mathrm{pc}^{-2}$ and a total mass within 200 pc radius of the order of $\sim 10^9\,M_\odot$. A correlation analysis among the derived parameters shows that the central CO-line intensity is positively correlated with the central SMD, which suggests that the deeper is the gravitational potential, the higher is the molecular gas concentration in the nuclei, regardless of the morphological types.

Key words: galaxies: dynamics and mass — galaxies: molecular gas — galaxies: rotation curves — galaxies: Virgo cluster of — ISM: CO line

1. Introduction

Rotation curves (RC) are among most basic tools used to investigate the dynamics of galaxies and to derive the mass distribution. Extensive observations have been achieved in radio (H I: Bosma 1981a,b) and optical wave ranges (Hα: Rubin et al. 1980, 1982, 1985, 1999; Mathewson et al. 1992, 1996). Outer flat RCs were noticed in early studies (Rubin et al. 1980, 1982, 1985; Bosma 1981a,b), and are often used to estimate the mass distributions in disks and halos (Rubin et al. 1985; Kent 1986; Persic, Salucci 1995; Persic et al. 1996).

Detailed studies of central RCs of spiral galaxies started only recently (Sofue 1996, 1997; Sofue et al. 1999; Bertola et al. 1998; Rubin et al. 1997, 1999; Sofue, Rubin 2001 for a review). In our studies of nearby galaxies, we have shown that the RCs generally rise steeply in the galaxy centers, and reach rotation velocities as high as ~ 100–$300\,\mathrm{km\,s}^{-1}$ within radii of 100–200 pc, indicating massive central cores (Takamiya, Sofue 2000). Based on these results, we conducted new observations of the central rotation properties of the Virgo CO rich spirals with a high accuracy using the Nobeyama Millimeter-wave Array (NMA) in the ^{12}CO (J = 1–0) line (Sofue et al. 2003a; hereafter Paper I).

Rotation curves have been derived using position–velocity diagrams (PVD) by optical (Hα, N II) and radio (CO, H I) line observations. There have been several methods to derive RCs from PVDs. The traditional method is to trace intensity-weighted velocities (Warner et al. 1973); the most popular method is to trace peak-flux ridges in PVDs (Rubin et al. 1985; Mathewson et al. 1992). These methods have given good results for the outer regions of galaxies and for mildly tilted galaxies with sufficiently high spatial resolutions. Other methods are the terminal-velocity method used for our Galaxy (Clemens 1985), and the envelope-tracing method (ETM) (Sofue 1996, 1997; Olling 1996), which trace the envelope velocities on PVDs, and correct for any interstellar velocity dispersion and for instrumental resolutions. The ETM gives better results for the central regions and for highly inclined and edge-on galaxies. We have applied this method to intermediately inclined galaxies to obtain central-to-outer RCs of many spiral galaxies (Sofue 1996; Sofue et al. 1999).

These various methods have been the most practical ways to derive RCs from PVDs. However, they do not necessarily give good results for the central regions, where the PVDs show a large intrinsic velocity width and a high interstellar velocity dispersion. The central PVDs also suffer strongly from the smearing effect due to finite beam sizes and finite slit widths. In fact, the RCs derived by these methods cannot reproduce the observed PVDs in the innermost regions of galaxies, when they are convolved with the observed intensity distributions (Takamiya, Sofue 2002). In order to resolve these problems, we have developed a new iteration method, which we describe in detail and apply to our new data in section 2.

Not only the methods, but also the properties of the used lines and observational conditions, have limited the accuracy of the central RCs. The resolutions in H I observations were usually tens of arcseconds, insufficient to resolve the central disks; also the H I gas is often deficient at the centers. Optical lines are severely absorbed by the central dusty disks, particularly in cases of edge-on galaxies. Optical spectra are severely

contaminated by the bright continuum emission of the bulge and nucleus. The Hα emission is often superposed by a broad absorption line due to the Balmer wing, and is often superposed by an extremely broad emission line due to Seyfert activity.

In this context, we have stressed that the CO line would be an ideal tool to investigate the central kinematics and RCs because of the following advantages (Sofue 1996, 1997; Sofue et al. 1999): (1) CO gas is strongly concentrated in the central region. (2) The CO gas has a much smaller intrinsic velocity dispersion than stars, so that the velocities manifest the rotation. (3) Even though each molecular clump is optically thick for the CO line, the LVG (large velocity gradient; Goldreich, Kwan 1974) assumption allows us to regard the entire gas as being transparent for studying the kinematics. (4) High angular resolution can be achieved by mm-wave interferometry. (5) High velocity resolution can be achieved by radio spectrometers using the heterodyne technique. (6) High sensitivity can be achieved by large-aperture telescopes and interferometers.

The Virgo high-resolution CO survey (ViCS) was conducted in order to obtain a high angular- and spectral-resolution database for a large number of CO-bright Virgo Cluster galaxies in the ^{12}CO (J = 1–0) line using the Nobeyama Millimeter-wave Array (NMA) of NRO.[1] The major scientific motivation was to investigate detailed central kinematics of the galaxies, particularly innermost RCs from an analysis of PVDs across the nuclei, and to derive the central mass distributions. The advantage to observe the Virgo members is the identical distance of 16.1 Mpc based on the Cepheid calibration (Ferrarese et al. 1996). Thus, 1″ corresponds to 78 pc, and 1 kpc corresponds to 12.″8.

The observations were obtained during the course of a long-term project in the winter seasons from 1999 December through 2002 April in the AB (longest base lines), C (medium) and D (short base lines) array configurations of the NMA. The resultant spatial resolution was 2″ to 4″, and the velocity resolution was 10 to 20 km s^{-1}. Detailed descriptions of the survey together with the observational parameters and reduction procedure are given in Paper I (Sofue et al. 2003a).

In this paper we use the observed PVDs to derive RCs by applying the iteration method (Takamiya, Sofue 2002), and calculate the radial distributions of the surface-mass density (SMD) by applying the SMD-deconvolution method described in Takamiya and Sofue (2000).

2. Rotation Curves Using the Iteration Method

2.1. Iteration Method

RCs have been derived from the observed PVDs and, thus, should be able to reproduce the original PVDs when convolved with intensity profiles. The iteration method (Takamiya, Sofue 2002) determines a RC so that it becomes consistent with the observation on PVD-basis. We describe the iteration procedure below. The algorithm is illustrated by a flow chart in figure 1. We assume axisymmetry of a galactic disk throughout the iteration.

[1] NRO (Nobeyama Radio Observatory) is a branch of the National Astronomical Observatory, operated by the Japanese Ministry of Education, Culture, Sports, Science and Technology.

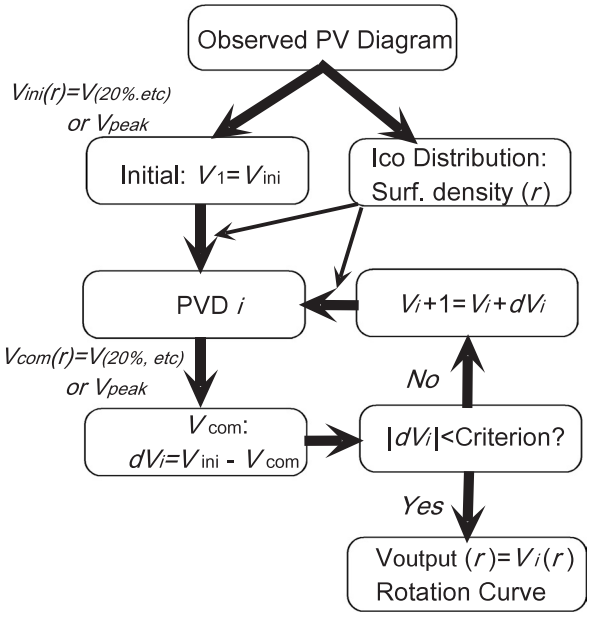

Fig. 1. Algorithm of the iteration method to derive an exact rotation curve from an observed position–velocity diagram (Takamiya, Sofue 2002).

Before the iteration, we define a reference RC ($V_{\rm ref}$) and a three-dimensional intensity distribution ($I_{\rm ref}$) in a galaxy disk. Here, $V_{\rm ref}$ is defined as the radial velocity profile traced at the 20%-level envelope of the peak flux in the PV$_{\rm obs}$. Here, PV$_{\rm obs}$ denotes the observed PVD, The intensity, $I_{\rm ref}$, is assumed to have the form

$$I_{\rm ref}(r, z) = A\Sigma(r)\,{\rm sech}^2(z/h_z), \tag{1}$$

where $\Sigma(r)$ is obtained by integrating PV$_{\rm obs}$ along the velocity at each radius, ${\rm sech}^2(z/h_z)$ is a model z-direction structure, and A is a normalization constant. We assume a scale height of h_z = 100 pc, and the intrinsic velocity dispersion of the ISM is assumed to be isotropic and is taken as σ_v = 10 km s^{-1}. An initial guess of RC (V_0) is set to be $V_0 = V_{\rm ref}$. Then, the iteration proceeds as follows. In the following, model PVD and RC value at the i-th iteration are denoted by PV$_i$ and V_i, respectively.

Step 1: Constructing a model galaxy by convolving V_i and $I_{\rm ref}$ while taking σ_v into account.

Step 2: Virtually observing the model galaxy to obtain PV$_i$ under the same conditions (slit-width, resolution, inclination, etc.) that PV$_{\rm obs}$ was observed.

Step 3: Determining a temporal RC ($V_{\rm t}$) by tracing the 20%-level envelope of the peak flux in PV$_i$.

Step 4: Calculating the difference

$$\Delta V_i \equiv V_{\rm ref} - V_{\rm t}, \tag{2}$$

which should be close to the difference between V_i and the real RC that we want to obtain.

Step 5: Applying an iteration termination criteria,

$$|\Delta V_i| < \sigma_{\rm tol}, \tag{3}$$

where $\sigma_{\rm tol}$ is an arbitrary tolerance velocity; we set it as $\sigma_{\rm tol}$ = 20 km s^{-1}. If the criterion is not satisfied, we go

Table 1. Adopted center positions, systemic velocities, and parameters for RC-PVD iteration.

Galaxy	R.A. (J2000)	Dec. (J2000)	$V_{\rm sys,lsr}$ ($\rm km\,s^{-1}$)	Inclination (deg)	Beam size ($''$)	Slit width ($''$)
NGC 4192	$12^{\rm h}13^{\rm m}48\overset{\rm s}{.}29$	$+14^{\rm d}54'01\overset{''}{.}9$	−127.3	74.0	2.0	3.0
NGC 4254	$12^{\rm h}18^{\rm m}49\overset{\rm s}{.}61$	$+14^{\rm d}24'59\overset{''}{.}6$	2410.8	28.0/42.0	2.5	3.0
NGC 4303	$12^{\rm h}19^{\rm m}21\overset{\rm s}{.}67$	$+04^{\rm d}45'03\overset{''}{.}7$	1557.9	25.0	2.5	3.0
NGC 4402	$12^{\rm h}26^{\rm m}07\overset{\rm s}{.}44$	$+13^{\rm d}06'44\overset{''}{.}7$	216.4	75.0	2.5	3.0
NGC 4419	$12^{\rm h}26^{\rm m}56\overset{\rm s}{.}40$	$+15^{\rm d}02'50\overset{''}{.}2$	−188.6	67.0	3.0	3.0
NGC 4501	$12^{\rm h}31^{\rm m}59\overset{\rm s}{.}12$	$+14^{\rm d}25'13\overset{''}{.}3$	2261.1	58.0	4.5	3.0
NGC 4535	$12^{\rm h}34^{\rm m}20\overset{\rm s}{.}35$	$+08^{\rm d}11'52\overset{''}{.}2$	1966.3	43.0	3.0	3.0
NGC 4536	$12^{\rm h}34^{\rm m}27\overset{\rm s}{.}08$	$+02^{\rm d}11'17\overset{''}{.}0$	1801.7	67.0	2.2	3.0
NGC 4548	$12^{\rm h}37^{\rm m}57\overset{\rm s}{.}47$	$+14^{\rm d}13'18\overset{''}{.}0$	464.9	37.0	2.3	3.0
NGC 4569	$12^{\rm h}36^{\rm m}49\overset{\rm s}{.}79$	$+13^{\rm d}09'48\overset{''}{.}7$	−195.8	63.0	4.0	3.0
NGC 4654	$12^{\rm h}41^{\rm m}25\overset{\rm s}{.}59$	$+13^{\rm d}24'03\overset{''}{.}2$	1051.4	52.0	5.0	3.0
NGC 4689	$12^{\rm h}50^{\rm m}15\overset{\rm s}{.}86$	$+13^{\rm d}29'27\overset{''}{.}4$	1614.8	30.0	5.0	3.0

to Step 6. If the criterion is satisfied, the iteration terminates, and the resultant RC is V_i.

Step 6: Calculating V_{i+1} for the next iteration step $(i + 1)$ as

$$V_{i+1} \equiv V_i + \Delta V_i, \tag{4}$$

and we go back to Step 1.

We made some modifications to the original method of Takamiya and Sofue (2002). In the original method, only the radial velocity profiles at the 20%-level envelope in $\rm PV_{obs}$ and $\rm PV_{\it i}$ were considered. We further take the 20, 40, 60, 80, 100%-level envelopes ($V^l_{\rm ref}$ and V^l_i; l = 20, 40, 60, 80, 100%), and replace equation (2) by

$$\Delta V = \sum_l g_l \cdot (V^l_{\rm ref} - V^l_{\rm t}), \tag{5}$$

where weights g_l satisfy $\sum_l g_l = 1$. We usually set $g_1 = g_2 = \cdots = g_l$, while some g_l's are occasionally set to be zero in cases that those V^l are ill-determined owing to noise. This modification avoids any instability occurred in the iteration that comes from fluctuations on the 20%-level envelopes. When $g_l = 1$ for l = 20% and 0 for the others, equations (2) and (5) become identical.

2.2. *Center Positions*

The center positions are adopted from Paper I, where we applied the task **GAL** in the AIPS reduction package, which fits the velocity field (the first moment map of the RA–Dec–Velocity cube), by a Brandt rotation curve (Brandt, Scheer 1965). Table 1 lists the thus-obtained dynamical centers and systemic velocities. In most cases the observed centers coincided well with the observed centers within one arcsecond. However, some deviation was found for NGC 4254 and NGC 4402, and we reset the centers of these galaxies to the determined dynamical centers.

The **GAL** fit also gave the inclination and position angle of the inner disk. However, these quantities are dependent on the streaming motions superposed on the circular rotation, which are not negligible in the central regions. Therefore, we adopted the inclination and position angles of the whole galaxies determined from optical images of wider disks. In table 1 we list the adopted inclination angles taken from Paper I and the literature therein. We adopt these values for constructing PVDs and rotation curves.

2.3. *Position–Velocity Diagrams*

In order to obtain PVDs of the observed galaxies, we first rotated the data cube in (RA, Dec, Velocity) to (X, Y, V), so that the first axis X represents the distance in the major axis direction, the second axis Y the distance along the minor axis, and the third axis V the radial velocity. We then transposed it to a cube with the axes (X, V, Y). Here, each (X, V) plane represents a PVD sliced at a distance Y from the minor axis.

The PVD along the major axis was obtained as that at $Y = 0$. In order to increase the signal-to-noise ratio, we averaged several diagrams within $Y = \pm 1\overset{''}{.}5$ from the major axis, or those within a slit of $3''$ wide across the dynamical center. However, the beam sizes were comparable to, or greater than, the slit width as shown in table 1. The effective spatial resolutions in the PVDs are, therefore, (beam width^2 + slit width^2)$^{1/2}$, which are typically a few arcseconds. The upper diagrams of figure 2 show the thus-constructed observed PVDs along the major axes across the dynamical centers after correcting for the inclinations of galaxy disks. The intensities are gray-scaled, so that the maximum intensity is in black, and the minimum in white. The distance scale is in arcseconds, where $1'' = 78$ pc, and 1 kpc = $12\overset{''}{.}8$ for the assumed distance of 16.1 Mpc.

2.4. *Rotation Curves*

We applied an iteration method to the observed PVDs, and obtained rotation curves for 12 galaxies, as listed in table 1. Both sides of each PVD along the major axis were fitted independently. The obtained RCs are shown in the lower diagrams of figure 2, where we show the reproduced PVDs calculated by convolving the RCs with the observed intensity distributions. In most cases, the convolved PVDs well mimic the observations. We then averaged the absolute values of the RCs from both sides for each galaxy, and obtained rotation curves as a function of the radius. We adopted these RCs for the inner regions, and combined them with outer optical RCs from Rubin et al. (1999) to obtain RCs covering wider regions. We

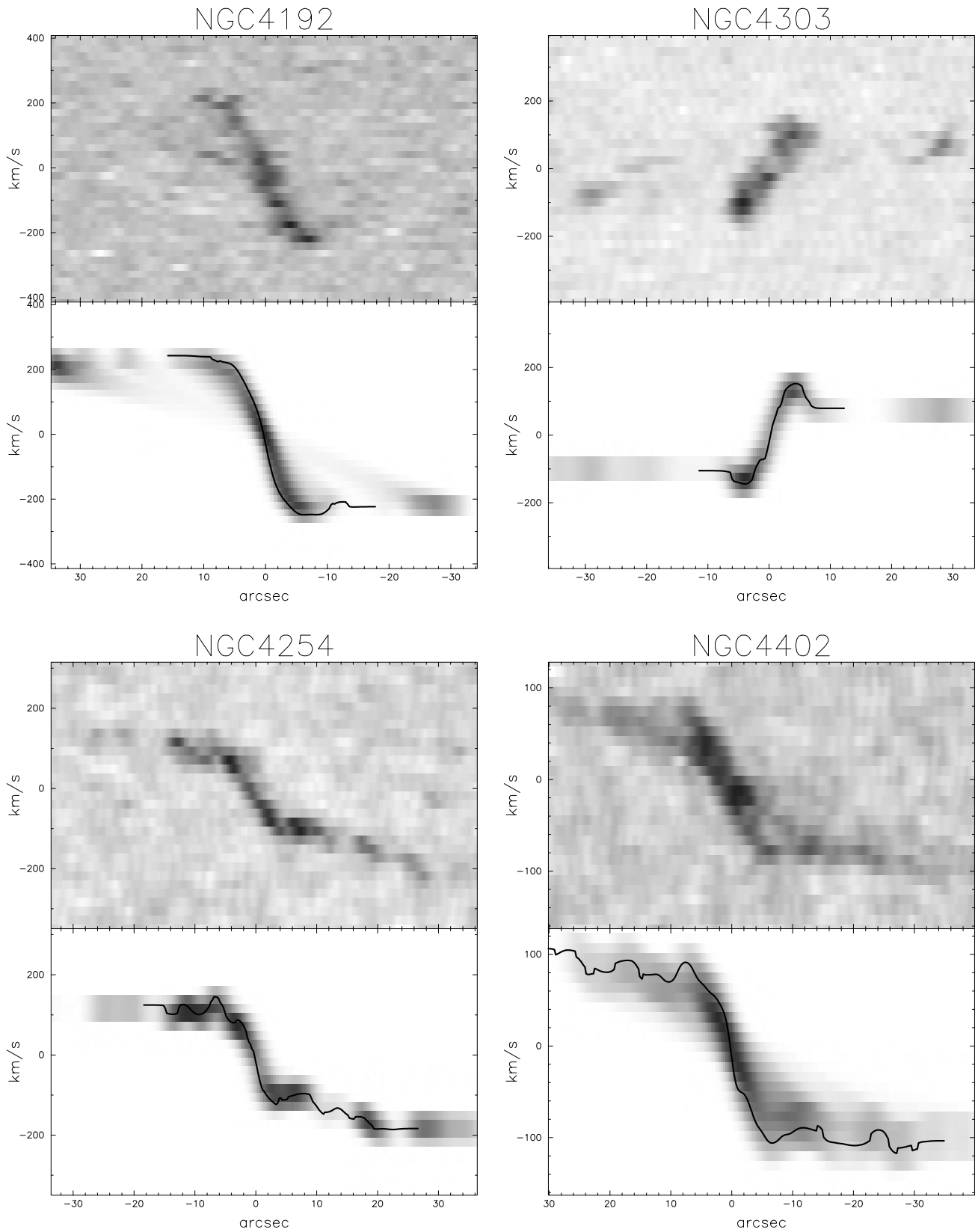

Fig. 2. (Upper panels:) Observed PVDs along the major axes after correcting for the inclination of galaxy disks. (Lower panels:) Obtained rotation curves by the iteration method, and reproduced PVDs by convolving the RCs with observed intensity distributions. Here, $1''$ = 78 pc and 1 kpc = $12\farcs8$ for the adopted Virgo distance of 16.1 Mpc.

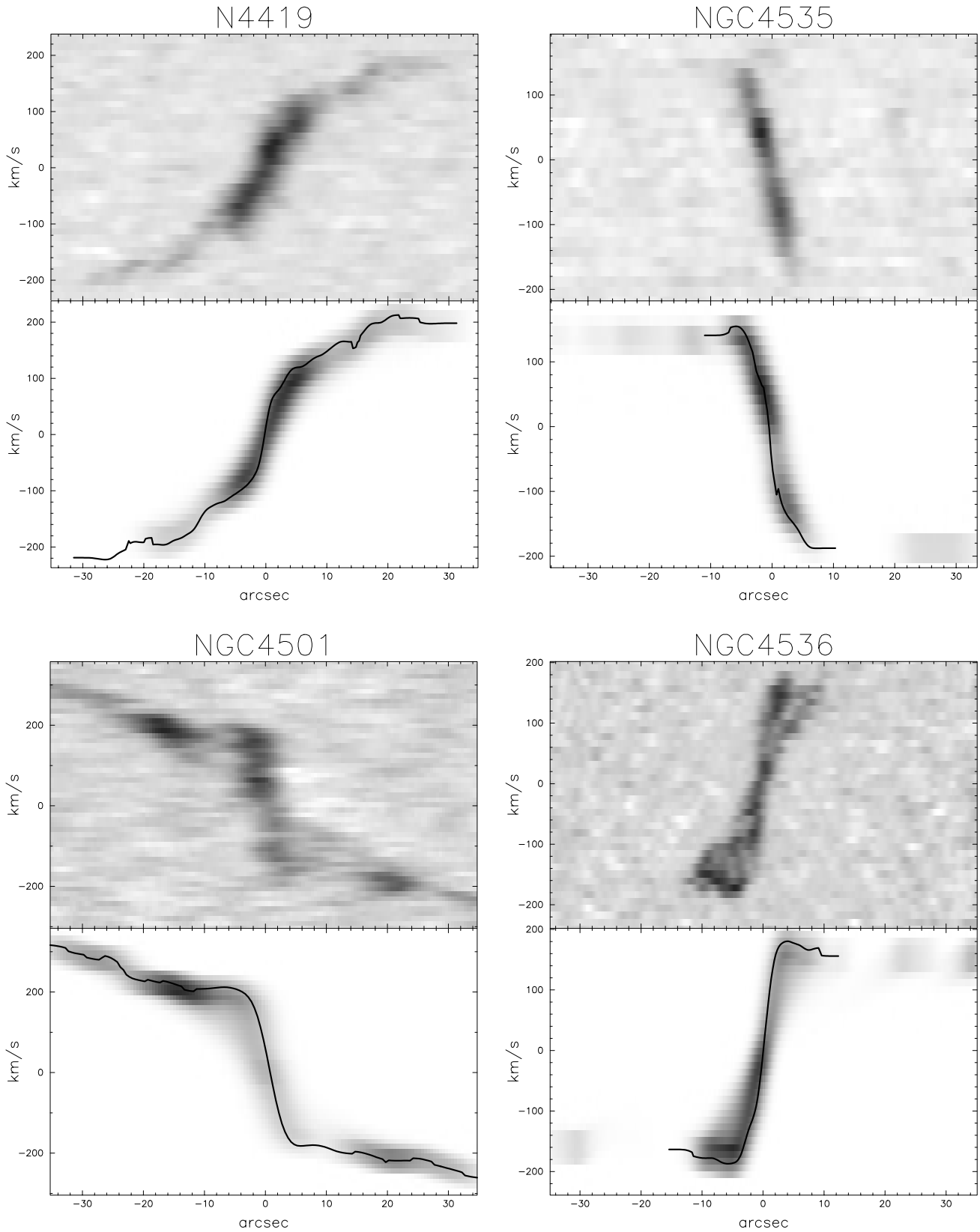

Fig. 2. (Continued.)

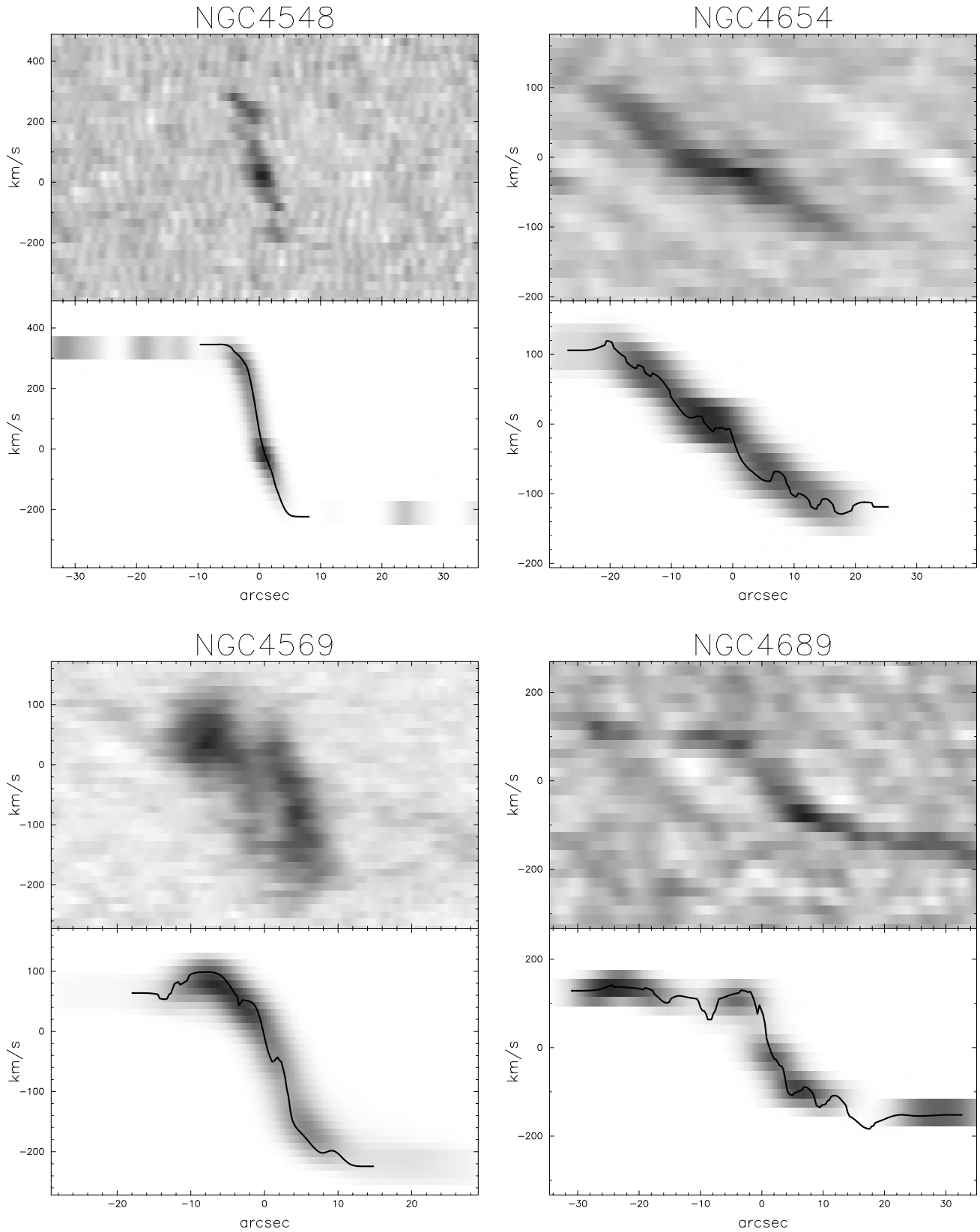

Fig. 2. (Continued.)

also used outer RCs from Sofue et al. (1999) for NGC 4303 and NGC 4569 for larger radii, where both optical and H I data have been combined. When there were two or more observations from the literature, we took the average. Since the inclination angles used in the literature are not necessarily the same as those used in our analysis, we corrected them to the same inclination angles as in table 1. Figure 3a shows the combined RCs of the Virgo galaxies, where the inner CO RCs from the present observations are drawn by thick lines. In figure 3b we plot all RCs in one diagram in order to see their general property.

The resultant RCs in figure 3 indicate a very steep rise in the central few arcsec regions, or in radii of 100 to 200 pc. The steep rise near the center is remarkable when we compare with those from Hα and H I observations. Note, however, that fluctuations of about $\pm 10\,\mathrm{km\,s^{-1}}$ superposed on the RCs are not real, which arise mainly from patchy distributions of emission in the PVDs.

3. Mass Distributions

The radial distribution of the surface-mass density (SMD), $\sigma(R)$, can be calculated directly from a rotation curve (Takamiya, Sofue 2000; and the literature therein). We may assume that the 'true' mass distribution in a real disk galaxy will be in between the two extreme cases, spherical and flat-disk distributions, as discussed in detail in Takamiya and Sofue (2000).

3.1. Spherical Mass Distribution

If we assume that the mass distribution is spherically symmetric, the SMD, $\sigma_{\rm S}(R)$, at radius R is calculated by

$$\sigma_{\rm S}(R) = 2\int_0^\infty \rho(r)\,dz, \tag{6}$$

$$= \frac{1}{2\pi}\int_R^\infty \frac{1}{r\sqrt{r^2-R^2}}\frac{dM(r)}{dr}\,dr. \tag{7}$$

Here, R, r, and z are related by $r=\sqrt{R^2+z^2}$; $\rho(r)$ the spatial density, and $M(r)$ is the mass inside radius r, given by

$$M(r) = \frac{rV(r)^2}{G}, \tag{8}$$

where $V(r)$ is the rotation velocity at r given by the rotation curve.

Note that the equation gives an underestimated mass at $R\sim R_{\rm max}$ because of an edge-effect that the integration is done only up to a maximum radius of observation, $R_{\rm max}$, instead of infinitely large R. However, this edge effect is negligible for the calculated result within a radius slightly smaller than $R_{\rm max}$, because the factor $(\sqrt{r^2-R^2})^{-1}$ rapidly diminishes as r gets away from R.

3.2. Flat-Disk Mass Distribution

If we assume that the galaxy comprises an infinitely thin flat disk, the SMD, $\sigma_{\rm D}(R)$, can be calculated by solving Poisson's equation:

$$\sigma_{\rm D}(R) = \frac{1}{\pi^2 G}\left[\frac{1}{R}\int_0^R \left(\frac{dV^2}{dr}\right)_x K\left(\frac{x}{R}\right)dx + \int_R^\infty \left(\frac{dV^2}{dr}\right)_x K\left(\frac{R}{x}\right)\frac{dx}{x}\right], \tag{9}$$

where K is the complete elliptic integral, and becomes very large when $x\simeq R$ (Binney, Tremaine 1987).

When we calculate $\sigma_{\rm D}(R)$, we must take into account the following points. First, the equation is subject to the boundary condition $V(0)=V(\infty)=0$. Because we have only a few data points for the very central region, where the assumption $V(0)=0$ may not apply based on the data, the calculated result near the nucleus would not be reliable. Hence, in so far as the central ~ 100 pc is concerned, the spherical assumption will give a more reliable SMD. Second, the upper boundary of the integration of the second term is $R_{\rm max}$, where $V(R)$ is finite, instead of $R=$ infinity, where the equation assumed zero velocity. This leads to an overestimation of $\sigma_{\rm D}(R)$ at $R\simeq R_{\rm max}$, and the SMD near the outer edges will give an upper limit.

3.3. Distributions of the Surface-Mass Density

Figure 4a shows the thus-calculated SMDs for individual galaxies, where the thick dotted lines represent the results for a flat-disk assumption, and the thin full lines for a spherical assumption. Since the central masses of galaxies are considered to be dominated by spheroidal components, we may rely more on the SMDs from a spherical assumption. On the other hand the SMDs from the flat-disk assumption give better results for the outer regions, where the disk component dominates. Thus, in the following we discuss the properties of the SMD in the central regions inside $r\sim 1$ kpc based on the spherical assumption, and those for the outer disks at $r>1$ kpc based on the flat-disk assumption. In order to see their general property, we show all of the SMD profiles from the flat-disk assumption in one diagram in figure 4b, and those from the spherical assumption for the central 2 kpc in figure 4c.

In spite of the variety of galaxy types and the morphology of the molecular gas distributions (Sofue et al. 2003a), the SMDs appear to show a basic, principal structure as following:

(1) Central massive core: The mass distribution is highly peaked at the center, showing a core component with a scale radius of about 100 to 200 pc. Since the estimated radius is comparable to, or smaller than, the beam size, this component is likely to be not fully resolved, but may have a smaller radius. The calculated central SMDs amount to $\sim 10^4$–$10^5\,M_\odot\,\mathrm{pc^{-2}}$, which is, however, a lower limit for the finite resolution. The dynamical mass of this component within 200 pc radius is on the order of $\sim 10^9\,M_\odot$. In table 2 we list the determined SMDs at the centers and dynamical masses within radii of 200 and 500 pc.

(2) Bulge component: The SMD is then followed by a more gradually decaying profile at $r=0.2$–2 kpc with a scale radius of about 500 pc. This component is due to the central bulge. A typical case of distinct components is seen for NGC 4536. However, in some galaxies the bulge and core component are not clearly distinguished because of insufficient resolution.

(3) Disk component: The radial profiles at radii of $r\sim 2$ to ~ 7 kpc are approximately expressed by an exponentially

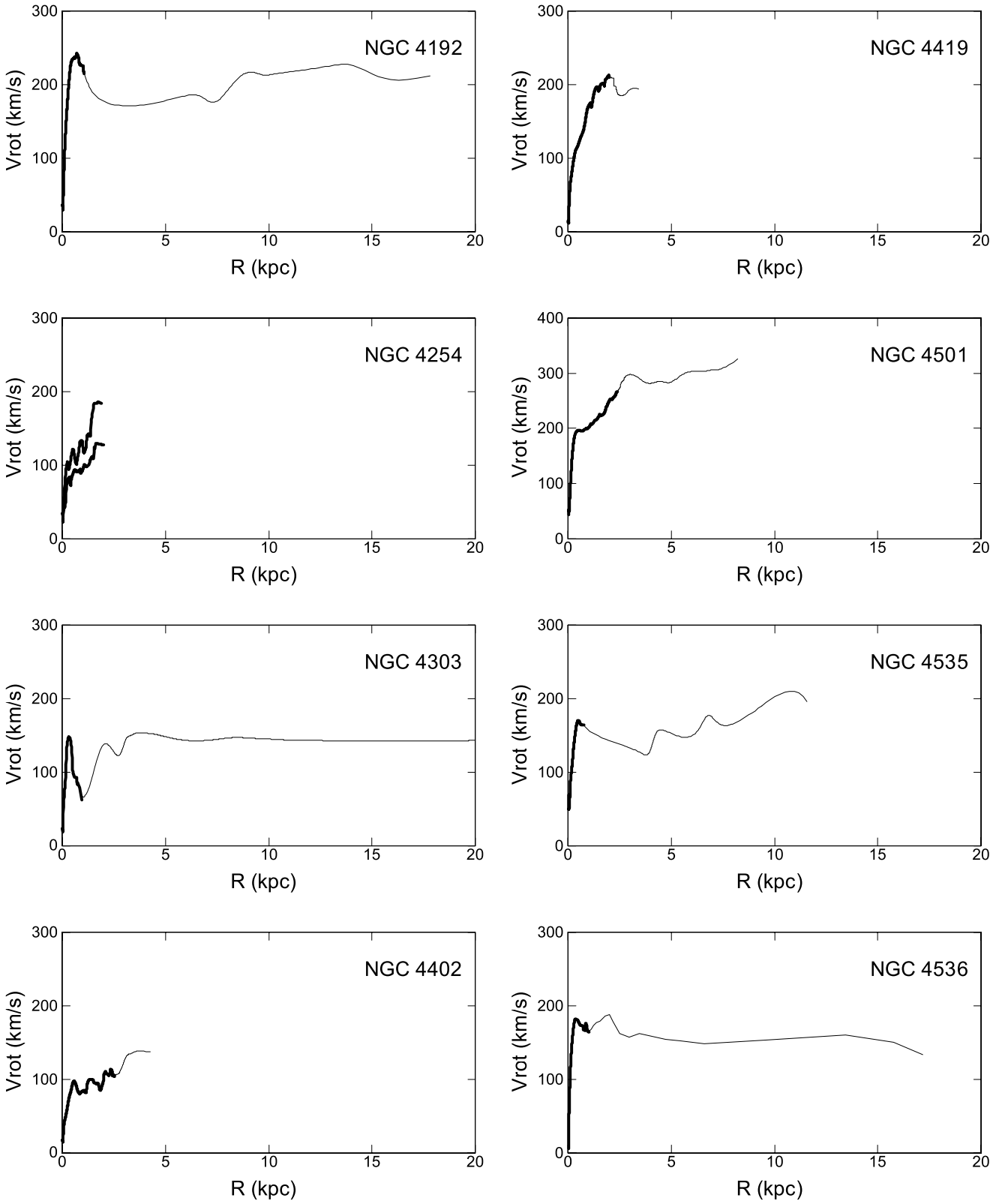

Fig. 3a. Rotation curves of the Virgo spiral galaxies obtained by the iteration method, combined with outer RCs from the literature (Rubin et al. 1999; Sofue et al. 1999), for which inclination angles are corrected to the same values as in table 1. The CO RCs from the present observations are drawn by thick lines.

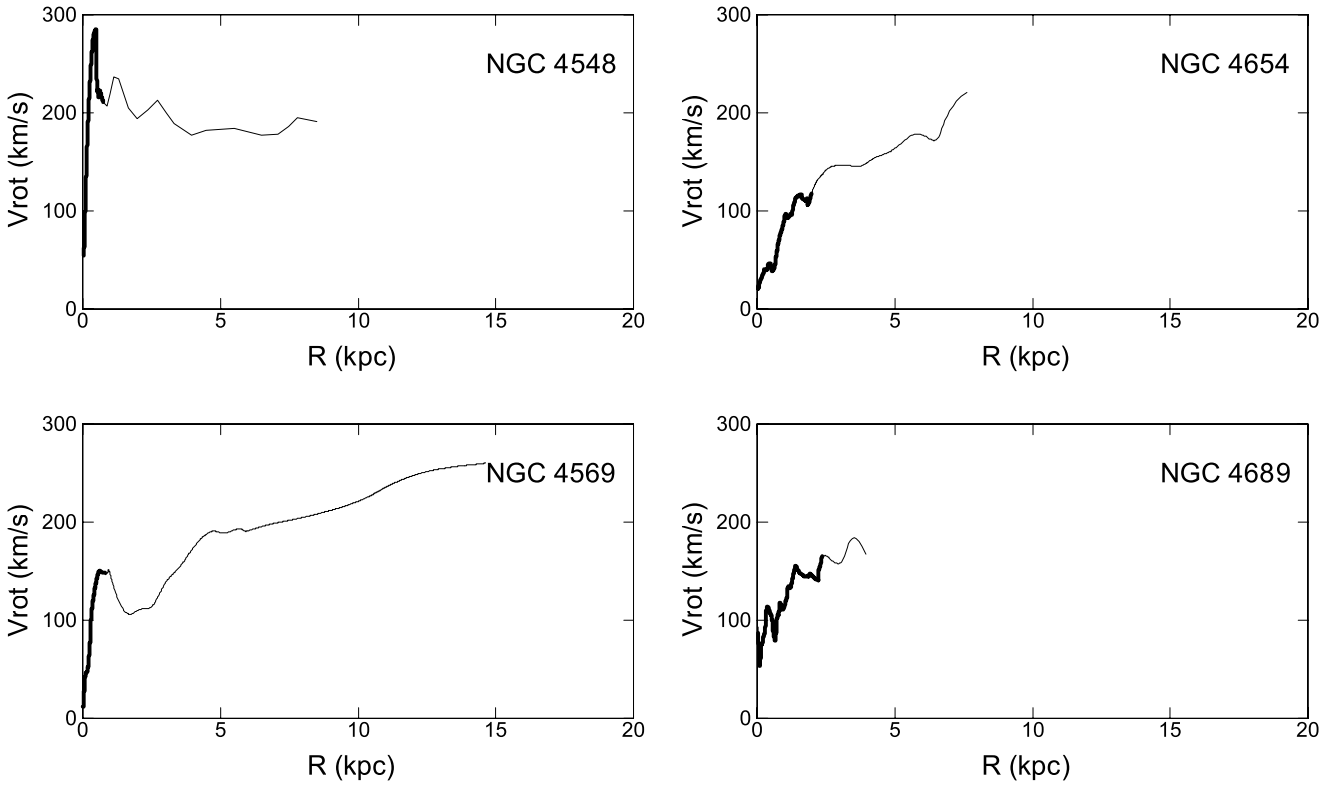

Fig. 3a. (Continued.)

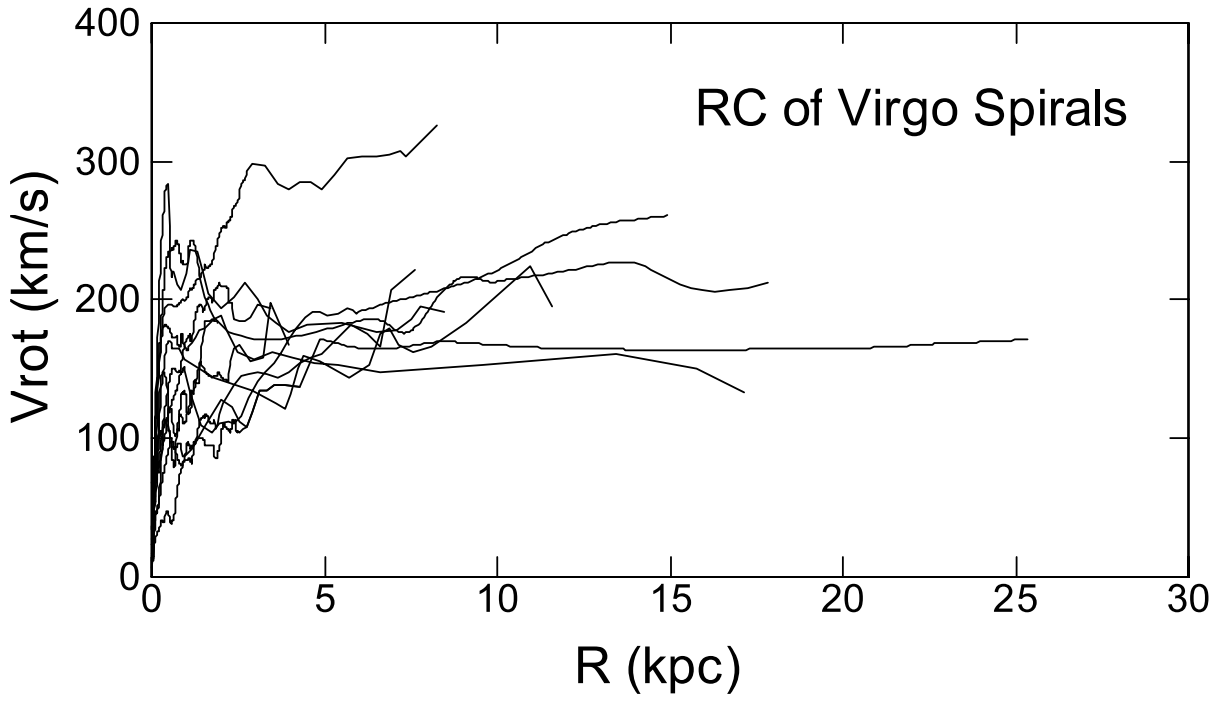

Fig. 3b. All rotation curves in one diagram.

decaying function of the scale radius of several kpc.

(4) Massive halo: At radii beyond $r \sim 7$–8 kpc, the SMD profile becomes more gently decreasing, indicating an excess over the exponential disk due to the massive halo. This is clearly seen in galaxies with RCs covering radii larger than ~ 10 kpc.

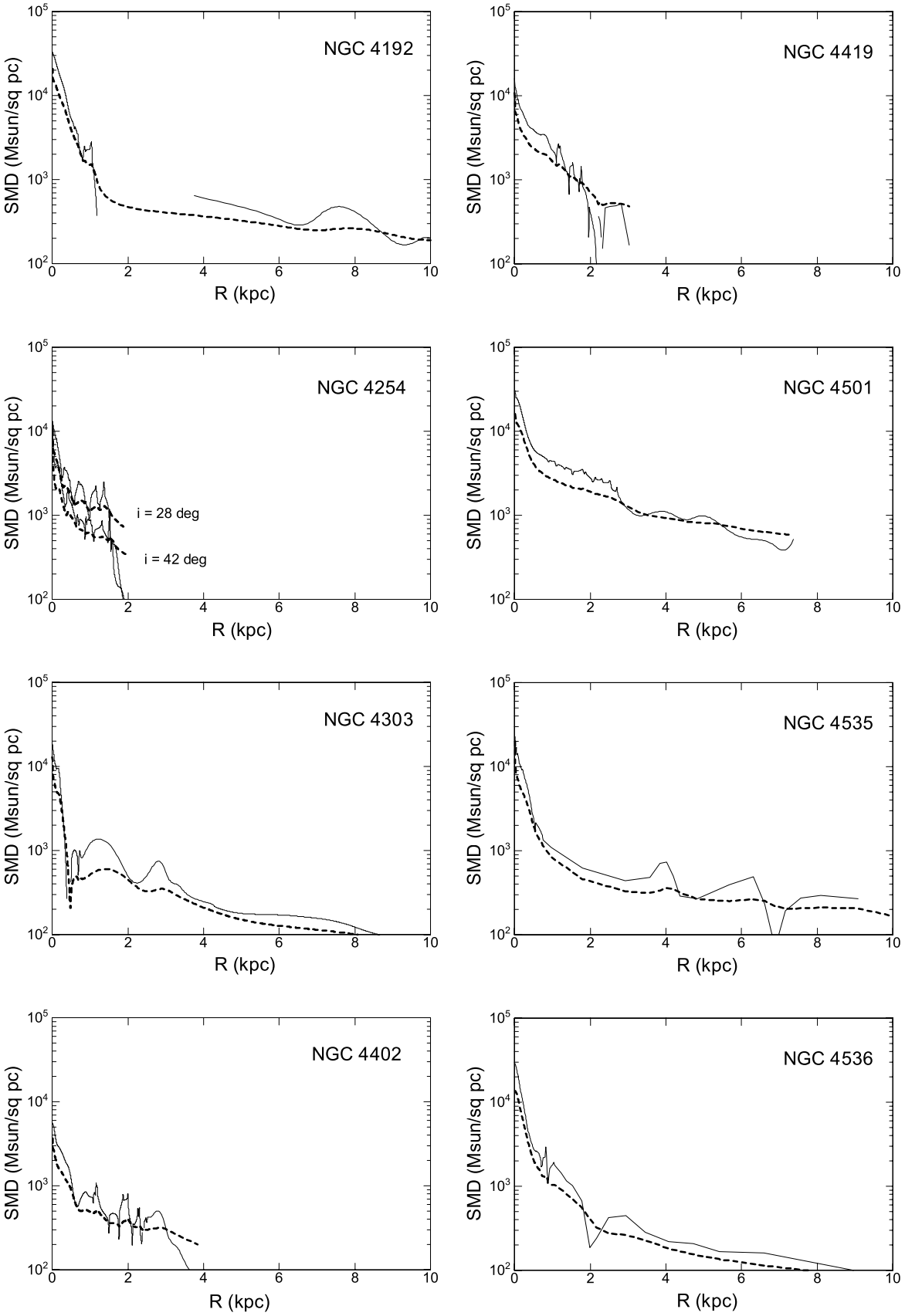

Fig. 4a. Radial profiles of the SMD (surface-mass density) of the Virgo spirals. Full lines are the results from spherical symmetry assumption, which are more reliable in inner region. Dashed lines are the result from flat-disk assumption, which are more reliable for the disk and outer region.

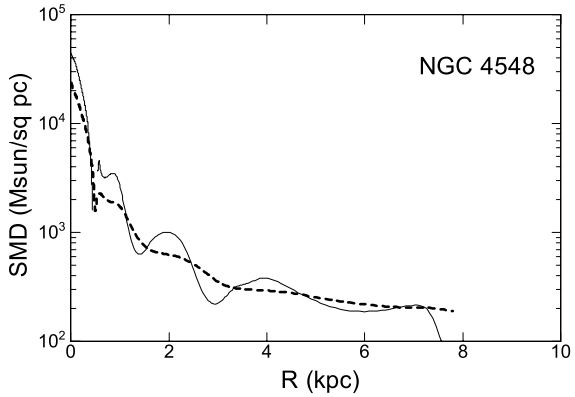

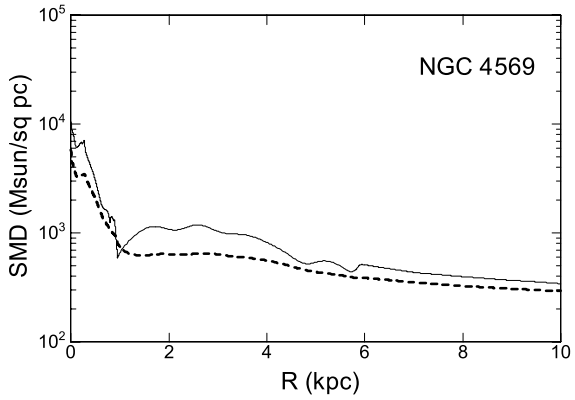

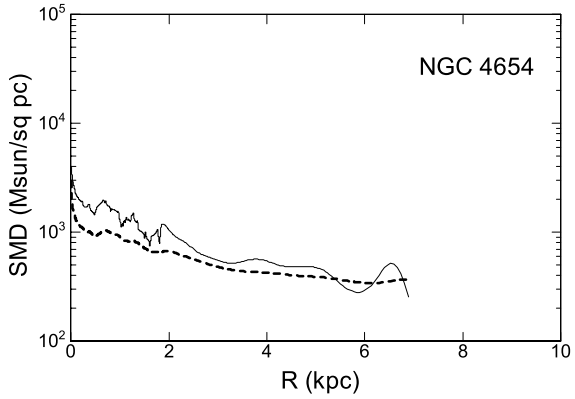

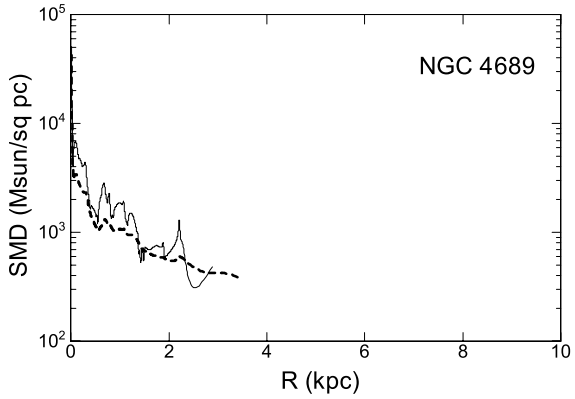

Fig. 4a. (Continued.)

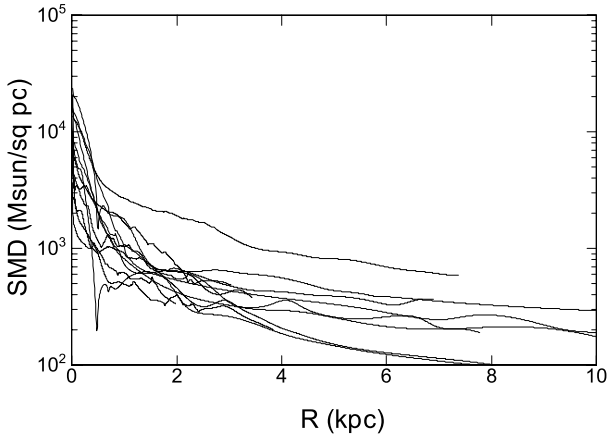

Fig. 4b. All SMD profiles from flat-disk assumption plotted in one diagram.

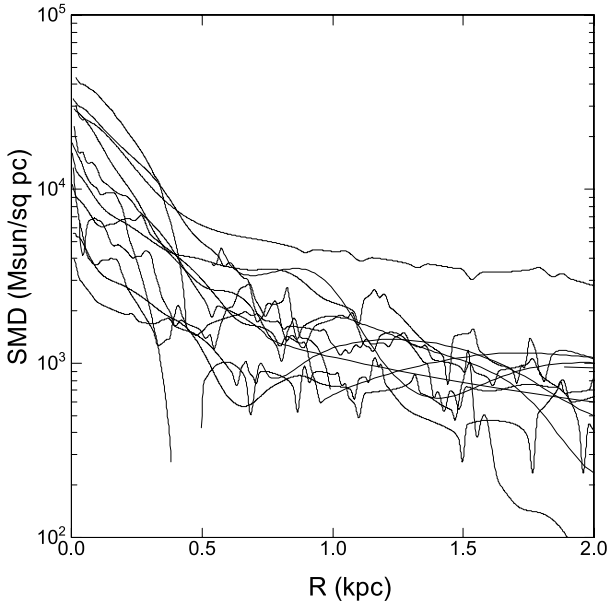

Fig. 4c. All SMD profiles from spherical assumption for the central 2 kpc region plotted in one diagram.

3.4. Correlation among Dynamical Properties

In table 2 we list the morphological types of the analyzed galaxies, their total B magnitude taken from NED, and the peak SMD at the center, Σ_c. We also list the dynamical masses within 200 pc and 500 pc radii from the dynamical centers, M_{200} and M_{500}, which were calculated by

$$M_R = R V_{\rm rot}^2 / G, \tag{10}$$

where $V_{\rm rot}$ is the rotation velocity given by the RCs, and G is the gravitational constant.

SMD vs. B magnitude: Figure 5a shows a plot of the center values of SMD (column 4 of table 2) against total B magnitude (column 3). There is a trend that brighter galaxies have a higher SMD. This is consistent with the fact that brighter galaxies have brighter bulges, as shown below for the bulge mass and the central SMD.

Table 2. Derived mass parameters and CO intensities.

(1) Galaxy	(2) Morphology	(3) $B_{\rm tot}$ (mag)	(4) Center SMD ($10^4\,M_\odot\,{\rm pc}^{-2}$)	(5) M_{200} ($10^9\,M_\odot$)	(6) M_{500} ($10^9\,M_\odot$)	(7) $I_{\rm CO,c}\cos i$ (K km s^{-1})	(8) $I_{\rm CO,p}\cos i$ (K km s^{-1})
NGC 4192	SAB(s)ab	10.95	3.4	1.16	6.42	73	96
NGC 4254	SA(s)c	10.44	1.4	0.32	1.64	60	82
NGC 4303	SAB(rs)bc	10.18	1.9	0.69	1.23	160	395
NGC 4402	Sb	12.55	0.5	0.14	1.03	5	58
NGC 4419	SB(s)a	12.08	1.3	0.34	1.67	100	229
NGC 4501	SA(rs)b	10.36	2.0	1.06	4.51	88	111
NGC 4535	SAB(s)c	10.59	2.0	0.57	3.36	200	275
NGC 4536	SAB(rs)bc	11.16	3.0	1.10	3.72	171	224
NGC 4548	SBb(rs)	10.96	4.2	1.92	6.92	38	98
NGC 4569	SAB(rs)ab	10.26	0.9	0.15	2.31	162	266
NGC 4654	SAB(rs)cd	11.10	0.35	0.06	2.06	10	27
NGC 4689	SA(rs)bc	11.60	0.75	2.98	0.13	12	21

(1) NGC number. (2) Morphological type from RC3. (3) Total B magnitude from NASA Extragalactic Database (NED). (4) Surface mass density (SMD) at the center. (5) and (6) Dynamical mass calculated by spherical assumption. M_{200} and M_{500} are masses within 200 and 500 pc radii, respectively. (7) CO intensity at the center calculated by ellipse fitting, taken from Paper I corrected for inclination. (8) Peak CO intensities in the observed first-moment maps, taken from Paper I corrected for inclination. Note that the CO peaks are near to the centers, but do not necessarily coincide with the center positions.

Mass vs. B magnitude: Figure 5b is a plot of the dynamical masses within radii of 200 pc (column 5 of table 2; filled circles) and 500 pc (column 6; diamonds) against the total B magnitude. The trend is the same as for SMD vs. B.

SMD vs. dynamical mass: Figure 5c plots the center SMD (column 4 of table 2) against the dynamical masses within radii of 200 pc (column 5; filled circles) and 500 pc (column 6; diamonds). There is a tight correlation between the mass and SMD, which are related as

$$\Sigma_{\rm c} \propto M_{200}^{0.8} \tag{11}$$

and

$$\Sigma_{\rm c} \propto M_{500}. \tag{12}$$

This correlation is naturally understood if the core radii of the central mass concentrations are not largely different among the galaxies.

Bulge mass vs. core mass: Since the rotation curves are nearly flat at radii from 0.2 kpc to 1 kpc in most galaxies, these dynamical masses and center SMD are positively correlated with the bulge mass, if the bulge radius is of the order of several hundred pc. Figure 5d plots the dynamical mass within 200 pc radius against that within 500 pc from the same table, which shows a linear correlation. The correlation between the center SMD and central mass within 200 pc with the surrounding dynamical mass would be somehow related to the correlation found for the masses of bulges and the central black holes (Kormendy, Richstone 1992).

3.5. *Correlation between the CO Concentration and the Dynamical Properties*

The seventh column of table 2 lists the integrated CO-line intensities at the centers determined by ellipse fitting, $I_{\rm CO,c}$, using the observed first moment maps, as taken from Paper I. The last column lists the peak CO intensities in the maps, $I_{\rm CO,p}$. The CO intensities are corrected for the inclination. Note that the CO intensity peaks do not necessarily coincide with the dynamical centers, which are, however, located near to the centers.

CO intensity vs. B magnitude: Figure 6a plots the central CO intensity (column 7 of table 2; circles) and the peak CO intensity (column 8; triangles) against the total B magnitude (column 3). There is a weak correlation between the B luminosity and the central as well as peak CO intensities: brighter galaxies have higher CO intensities.

CO intensity vs. SMD: An interesting correlation is found in figure 6b, where the center CO intensity (column 7 of table 2; circles) and peak CO intensity (column 8; triangles) are plotted against the center SMD (column 4). There is a clear correlation that the higher is the SMD, the higher is the peak and central CO intensities. This fact indicates that the deeper is the central gravitational potential, the more strongly the CO gas is concentrated in the nuclei.

4. Description of Individual Galaxies

We describe the properties of individual galaxies seen in their PVDs, rotation curves, and mass distributions. More general descriptions of individual galaxies including the CO intensity distributions and velocity fields, are given in Paper I.

4.1. *NGC 4192*

A bright CO intensity peak is observed at the center, and the galaxy is classified as a "central/single-peak" type (Paper I). The rotation characteristics appear to be normal with a high velocity rotation at ~ 500 pc. The rotation velocity, then, declines to a minimum at 3–4 kpc according to the outer rotation curve taken from the literature (Sofue et al. 1999). It is then followed by a flat rotation, which continues to the outer edge. The SMD shows that the central core and the bulge compose a single component, which is surrounded by an exponential disk.

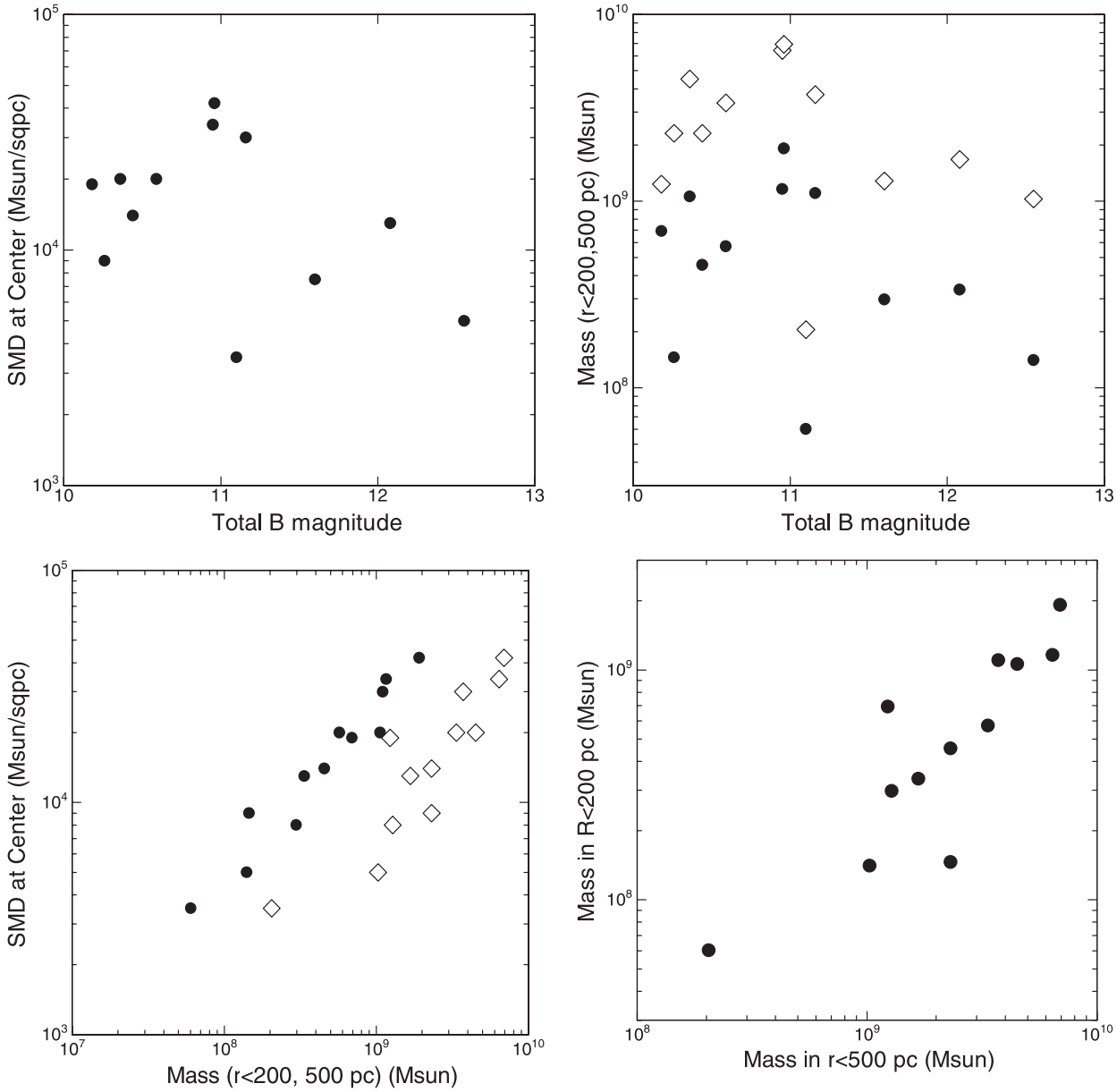

Fig. 5. (a) (Top left:) SMD at the centers plotted against the total B magnitude. (b) (Top right:) Dynamical masses within r = 200 pc (dots) and 500 pc (diamonds) against total B magnitude. (c) (Bottom left:) SMD against dynamical masses within r = 200 pc (dots) and 500 pc (diamonds). (d) (Bottom right:) Dynamical mass within r = 200 pc against that within 500 pc.

4.2. NGC 4254

The velocity field shows a regular spider pattern, indicating a circular rotation of the disk. The PVD and RC show a sharp rise of the rotation velocity in the central two arcseconds (150 pc), reaching a shoulder-like step at 100 km s^{-1}, the velocity then gradually increases to 150–200 km s^{-1}, depending on the inclination angle. Note that there are two possibilities of inclination angles, either 28° inferred from molecular gas disk or 42° from K-band images (Sofue et al. 2003b). The SMD clearly shows a massive core with a sharp peak, and a bulge component. They are surrounded by a disk component, while the disk part is uncertain for the limited coverage in the present data.

4.3. NGC 4303

The intensity distribution is classified as twin-peaks, and shows two prominent off-set bar ridges. Due to the non-circular motion, the PVD has a larger velocity dispersion compared to the other galaxies. The RC indicates a steep rise of rotation within a few arcseconds, but it is wavy at $r < 3$ kpc radius. Such wavy behavior of RC is typical for a barred galaxy (Sofue et al. 1999). Accordingly, the SMD behaves peculiar at 1 to 4 kpc, and no firm conclusion about the inner mass distribution can be obtained. However, the velocity field in the very central region within the radius of 300 pc shows a regular spider pattern, where a steep rise of rotation is observed. Hence, the central massive component shown in the SMD will be real, as well as

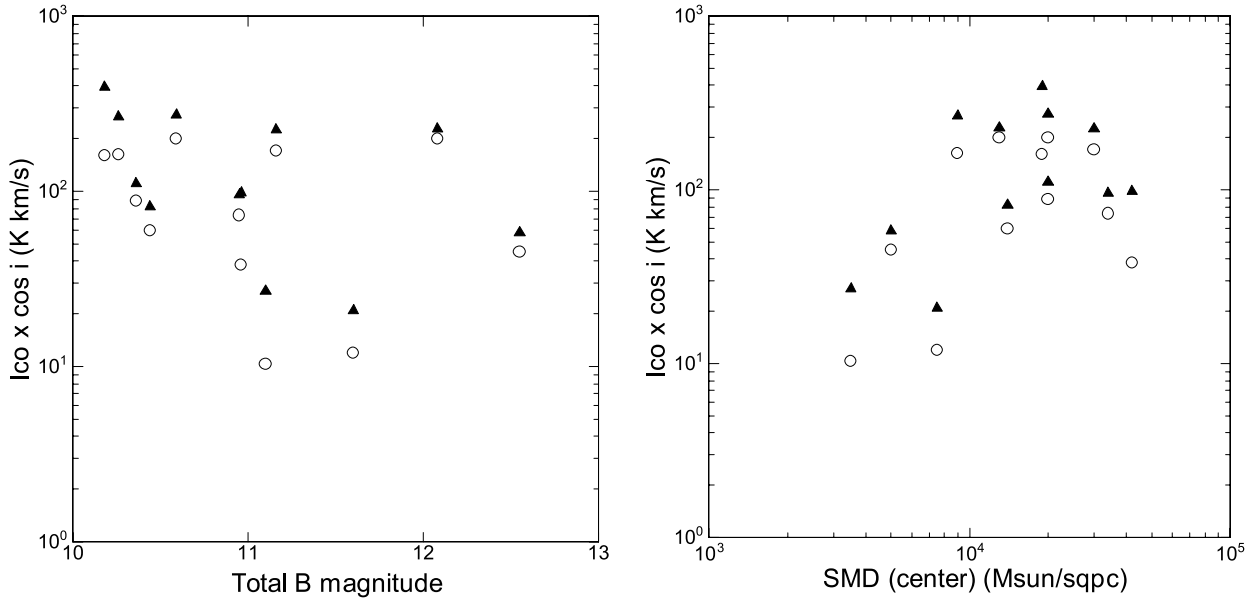

Fig. 6. (a) (Left:) Peak (triangles) and central (circles) CO intensities corrected for inclination angle plotted against total B magnitude. (b) (Right:) Peak (triangles) and central (circles) CO intensities against the central SMD.

that at $r > 5$ kpc.

4.4. NGC 4402

The CO intensity distribution shows a high-density nuclear disk of radius $\sim 10''$, which is surrounded by a more broadly distributed molecular disk with arm structures. The PVD and RC show steeply rising nuclear rotation, followed by a gradually rising outer disk rotation. The SMD indicates a sharp peak at the center, suggesting a massive core with a small-scale radius, while the present resolution is not sufficient. It is then surrounded by a bulge and disk components.

4.5. NGC 4419

The CO gas is strongly concentrated in the central $5''$ radius disk, showing a single-peak surrounded by outer disk. The central disk has steeply rising rotation, followed by a gradual rise of the disk component. The SMD comprises a central core plus bulge component, while the disk part does not show up because of insufficient radius coverage.

4.6. NGC 4501

A compact central peak and spiral arms are prominent in the intensity map. The velocity field is normal, showing a typical spider pattern. The PVD shows a central component superposed by a disk/arm component. The RC indicates a sharp central rise followed by a gradually rising part and flat outer rotation. The SMD indicates a central core plus a bulge and a disk.

4.7. NGC 4535

A high CO gas concentration is found at the center, and the velocity field is normal, showing a spider pattern. The PVD comprises a single ridge, and the RC rises steeply near the center, reaching a shoulder-like maximum, followed by a wavy frat part in the disk. The SMD indicates a core, bulge, and disk.

4.8. NGC 4536

This is also a single-CO peak galaxy with a typical spider velocity field. The PVD comprises two ridges, a central steeply rising component and a rigid-body-like disk component. The RC rises extremely steeply in the central 100 pc, reaching a maximum followed by a flat RC. SMD clearly shows three distinguishable components of the core, bulge, and disk.

4.9. NGC 4548

CO gas is concentrated in the central few arcsec region, and the intensity is weak. However, the PVD and RC show very high rotation in the central several hundred parsecs. Accordingly, the SMD shows a high-density central core, the bulge and disk components.

4.10. NGC 4569

CO gas is distributed in an elliptical ring of radius 500 pc, and the velocity field is complex, having anomalously high non-circular rotation. The PVD is complicated with two bright ridges having forbidden velocities. Our iteration program averaged the observed PVD, and obtained an RC, which gives only averaged rotation velocities. The SMD shows a bulge component and disk, while its detail in the central 1 kpc is not reliable because of the uncertainty in the RC determination.

4.11. NGC 4654

CO distribution is highly distorted and lopsided. The PVD shows a rigid-body ridge, and the RC is also gradually rising at $r < 2$ kpc. Accordingly, the SMD comprises only disk and bulge components with a slight enhancement due to a possible core component near the center.

4.12. NGC 4689

CO gas is broadly distributed with an amorphous morphology, but the velocity field is normal, showing a spider diagram. The CO intensity is weak and its distribution is patchy. PVD has a central ridge and an extended flat part. RC shows a sudden rise in the central ~ 100 pc to a velocity of $\sim 70\,\mathrm{km\,s^{-1}}$, and then gradually rises to a flat part. No clear compact component is seen in the SMD, while bulge and disk components show up.

5. Summary and Discussion

We analyzed the high-resolution CO-line survey of Virgo spirals obtained with the Nobeyama Millimeter-wave Array (Paper I) in order to derive dynamical parameters of the galaxies. The study of Virgo galaxies provided us with a unique opportunity to use the accurate, unambiguous Cepheid distance of 16.1 Mpc from the HST observations (Ferrarese et al. 1996). The high concentration of molecular gas in the centers and high spatial and velocity resolutions enabled us to determine the dynamical centers very accurately. From the data cube, we constructed position–velocity diagrams (PVDs) along the major axes across the dynamical centers.

By applying the new iteration method to derive exact rotation curves from PVDs as proposed by Takamiya and Sofue (2002), we determined rotation curves. The thus-obtained RCs can well reproduce the observed PVDs by convolving with the observed CO intensity distributions. We combined these RCs with outer disk RCs from the literature to obtain wider RCs. Except for a few cases, the RCs rise steeply near the center within the spatial resolution. Attaining a central peak or a shoulder after the rapid rise, the RCs are followed by gradually varying disk RCs, which are in general flat until the observed edge. Some galaxies like NGC 4303 and NGC 4659 with strong non-circular motion due to a bar show a wavy behavior at radii of ~ 1 kpc.

Using the thus-obtained RCs, we calculated the distributions of surface-mass density (SMD) as a function of radius based on the two extreme assumptions of spherical symmetry and flat-disk by applying the deconvolution method developed by Takamiya and Sofue (2000). Both the spherical and disk results agreed within a factor of two. The spherical assumption gives more reliable results for the innermost regions, where the bulge and core components are dominant. On the other hand, the flat-disk assumption gives better results for the disk and the outer regions, where the disk component dominates. In some galaxies for which wide RCs are available, a dark halo is clearly seen as an excess over the exponential SMD of the disk.

The SMDs generally have strong central condensation of mass on the scale radii of 100 to 200 pc, which we call the massive central core. The core radii are significantly smaller than those of bulges, whose scale radii are usually several hundred parsecs to one kpc. The dynamical masses of the massive cores within a radius of 200 pc are of the order of $10^9\,M_\odot$. Since the present spatial resolutions ($2''$–$4''$, 160–300 pc) are comparable to the supposed scale radii, we may have not fully resolved the core components. Therefore, the scale radii may still be smaller and, hence, the center SMD would be taken as a lower limit. The fact that the center SMD is roughly proportional to the dynamical mass within 200 pc radius (figure 5) suggests that the scale radii of the cores would not be largely scattered among the galaxies. The present results concerning the SMD distributions confirm our earlier results about massive cores (Takamiya, Sofue 2000; Sofue et al. 2001; Koda et al. 2002). Koda et al. (2002) argued in detail that the high-velocity rotation observed in the central region of NGC 3079 indeed manifests the central massive core with the deep gravitational potential.

An interesting correlation was found between the CO gas concentration around the nuclei and the central SMD. The higher is the central mass, the deeper is the potential, and the higher is the gas concentration. The observed galaxies are not dominated by barred galaxies and, moreover, the CO concentration is not dependent on the galaxy types. This fact implies that the often-mentioned inflow mechanism of molecular gas due to bar-driven angular momentum loss is not absolutely necessary. This is consistent with our recent results concerning the extremely high-density molecular core in NGC 3079, which was argued to be the consequence of a very deep potential, where the dense gas is maintained gravitationally stable due to high-velocity shears, and is suppressed from being fragmented to form stars (Sofue et al. 2001; Koda et al. 2002). The mechanism of the molecular gas concentration and its maintenance without suffering from being exhausted by star formation in a deep gravitational potential would be an interesting subject for the future.

The observations were performed as a long-term project from 1999 December till 2002 April at the Nobeyama Radio Observatory of the National Astronomical Observatories of Japan. We are indebted to the NRO staff for their help during the observations. We thank Dr. V. Rubin for making their rotation curves available in a tabular format. JK was financially supported by the Japan Society for the Promotion of Science (JSPS) for young scientists.

References

Bertola, F., Cappellari, M., Funes, J. G., Corsini, E. M., Pizzella, A., & Vega Betrán, J. C. 1998, ApJ, 509, L93
Binney, J., & Tremaine, S. 1987, Galactic Dynamics (Princeton: Princeton University Press)
Bosma, A. 1981a, AJ, 86, 1825
Bosma, A. 1981b, AJ, 86, 1791
Brandt, J. C., & Scheer, L. S. 1965, AJ, 70, 471
Clemens, D. P. 1985, ApJ, 295, 422
Ferrarese, L., et al. 1996, ApJ, 464, 568
Goldreich, P., & Kwan, J. 1974, ApJ, 189, 441
Kent, S. M. 1986, AJ, 91, 1301
Koda, J., Sofue, Y., Kohno, K., Nakanishi, H., Onodera, S., Okumura, S. K., & Irwin, J. A. 2002 ApJ, 573, 105
Kormendy, J., & Richstone, D. 1992, ApJ, 393, 559
Mathewson, D. S., Ford, V. L., & Buchhorn, M. 1992, ApJS, 81, 413
Mathewson, D. S., & Ford, V. L. 1996, ApJS, 107, 97

Olling, R. P. 1996, AJ, 112, 457
Persic, M., & Salucci, P., 1995, ApJS, 99, 501
Persic, M., Salucci, P., & Stel, F. 1996, MNRAS, 281, 27
Rubin, V. C., Burstein, D., Ford, W. K., Jr., & Thonnard, N. 1985, ApJ, 289, 81
Rubin, V. C., Ford, W. K., Jr., & Thonnard, N. 1980, ApJ, 238, 471
Rubin, V, C., Ford, W. K., Jr., & Thonnard, N. 1982, ApJ, 261, 439
Rubin, V. C., Kenney, J. D. P., & Young, J. S. 1997, ApJ, 13, 1250
Rubin, V. C., Waterman, A. H., & Kenney, J. D. P. 1999, ApJ, 118, 236
Sofue, Y. 1996, ApJ, 458, 120
Sofue, Y. 1997, PASJ, 49, 17
Sofue, Y., Koda, J., Kohno, K., Okumura, S. K., Honma, M., Kawamura, A., & Irwin, J. A. 2001, ApJ, 547, L115
Sofue, Y., Koda, J., Nakanishi, H., & Hidaka, M. 2003b, PASJ, 55, 75
Sofue, Y., Koda, J., Nakanishi, H., Onodera, S., Kohno, K., Okumura, S. K., & Tomita, A. 2003a, PASJ, 55, 17 (Paper I)
Sofue, Y., & Rubin, V. 2001, ARA&A, 39, 137
Sofue, Y., Tutui, Y., Honma, M., Tomita, A., Takamiya, T., Koda, J., & Takeda, Y. 1999, ApJ, 523, 136
Takamiya, T., & Sofue, Y. 2000, ApJ, 534, 670
Takamiya, T., & Sofue, Y. 2002, ApJ, 576, L15
Warner, P. J., Wright, M. C. H., & Baldwin, J. E. 1973, MNRAS, 163, 163